Article

Multifunctional nanoporous biocarbon derived from ginger: a promising material for CO_2 capture and supercapacitor

Jefrin M. Davidraj[1], C. I. Sathish[1,*] iD **, Vibin Perumalsamy[1], Vishnumaya Narayanan[1], Binodhya Wijerathne[2], Xiaojiang Yu[3], Mark B. H. Breese[3], Muhammad Ibrar Ahmed[1], Jiabao Yi[1,*]** iD **, Ajayan Vinu[1,*]** iD

[1]Global Innovative Centre for Advanced Nanomaterials (GICAN), College of Engineering, Science, and Environment, University Drive, The University of Newcastle, Callaghan, New South Wales 2308, Australia.
[2]School of Chemistry and Physics, Faculty of Science, Queensland University of Technology, Brisbane, QLD 4000, Australia.
[3]Singapore Synchrotron Light Source, National University of Singapore, Singapore 119260, Singapore.

*Correspondence to: Dr. C. I. Sathish, Global Innovative Centre for Advanced Nanomaterials (GICAN), College of Engineering, Science, and Environment, University Drive, The University of Newcastle, Callaghan, New South Wales 2308, Australia. E-mail: sathish.ci@newcastle.edu.au; Prof. Jiabao Yi, Global Innovative Centre for Advanced Nanomaterials (GICAN), College of Engineering, Science, and Environment, University Drive, The University of Newcastle, Callaghan, New South Wales 2308, Australia. E-mail: jiabao.yi@newcastle.edu.au; Prof. Ajayan Vinu, Global Innovative Centre for Advanced Nanomaterials (GICAN), College of Engineering, Science, and Environment, University Drive, The University of Newcastle, Callaghan, New South Wales 2308, Australia. E-mail: ajayan.vinu@newcastle.edu.au

Abstract

Nanoporous activated carbons derived from bio-waste are gaining consideration due to their exceptional potential for energy storage and CO_2 adsorption. Herein, we put forward a straightforward, low-cost method for preparing a highly efficient nanoporous biocarbon from ginger using solid-state activation approach. Ginger was pyrolyzed at various temperatures before activating using different amounts of KOH as an activator to produce nanoporous biocarbon. The prepared samples possess high specific surface areas and large pore volumes. By simply adjusting the pyrolysis temperature, the microporosity and surface oxygen functionalities can be finely tuned. The best sample exhibits a high Brunauer-Emmett-Teller-specific surface area of 2,330 m^2/g and a large pore volume of 1.10 cm^3/g and offers excellent specific capacitance of 244 and 119 F/g when tested in a three-electrode and two-electrode, at a current density of 0.5 A/g. Additionally, the optimized material demonstrates a high CO_2 uptake capacity of 4.87 mmol/g at ambient pressure and 25.8 mmol/g at 0 °C and 30 bar. These interesting adsorption

and energy storage performances of the nanoporous biocarbon underscore the potential of converting food waste into high-performance CO_2 adsorbents and supercapacitors.

Keywords: Bio-waste, porous activated carbon, CO_2 capture, supercapacitors, energy storage

INTRODUCTION

The ever-increasing demand for energy to meet the needs of the growing population has led to a continuous depletion of fossil fuels and a significant increase in greenhouse gas emissions. To address this dual challenge effectively, a combination of strategies is required: reducing CO_2 emissions and a revolutionary shift towards renewable energy technologies[1-3]. Consequently, tackling CO_2 emissions along with safe and efficient storage of energy using devices such as supercapacitors is of paramount importance. Therefore, it is crucial to rationally fabricate high-performance materials with specific characteristics for effective gas adsorption and high-performance energy storage[4-8].

Nanoporous carbons, particularly those derived from various biomass precursors, are one of the most extensively studied materials that have demonstrated great potential as CO_2 adsorbents and electrode materials for supercapacitors[9-13]. These materials are cost-effective, environmentally friendly and easily scalable to industry levels[14] and are characterized by high surface area, flexibility towards surface modification, strong adsorption capacity, and good thermal and chemical stability[8,15-22]. These characteristic features assert the utility of nanoporous carbons as adsorbents for CO_2 capture or electrodes for energy storage. However, the key to enhancing their practical utility lies not only in developing simple synthesis approaches that are both environmentally safe and economically viable but also in using the appropriate bio sources that can offer better surface properties and unique surface functionalities. For example, nanoporous biocarbon derived from high oxygen or nitrogen-containing biosources can offer heteroatom functionality on the surface of the materials, which is highly critical not only for adsorption but also for energy storage[7,23-31].

For this purpose, various biomass materials, including green wastes, serve as efficient starting materials for porous carbon synthesis. Pine cone flowers as a biomass source were converted to honeycomb-like activated porous carbon conducting scaffolds and coated on $Ni(OH)_2$ nanosheets to form composites, which exhibited excellent electrochemical properties[32]. The 3D N/O self-doped heteroatom honeycomb-like porous carbon was prepared from bio-waste oyster shells which exhibited exceptional electrochemical properties, including a high specific capacitance, large surface area, and good cycling stability. It was reported that the hierarchical structure and heteroatom doping are mainly responsible for their enhanced electrochemical performance[33]. Likewise, Nallapureddy *et al.* prepared graphitic carbon nano-onions (CNO) and hetero-atom-doped CNO from chicken fat oil biowaste through an oil-wick flame pyrolysis approach. This approach seems quite interesting as it offers a simple and economical synthesis process, resulting in CNO materials with good capacitance and h-CNO materials with even higher specific capacitance[34]. Utilizing these materials not only helps the efficient synthesis of porous carbon but also provides a concurrent safe disposal method for large amounts of such waste materials[35-38]. Among the various biomasses, ginger is produced in large quantities for food and fragrance purposes, one of the key seasoning elements for food cooking for its sweetness and pungent smell due to the existence of chemicals such as zingerone and gingerol. These chemicals may induce surface extra functionalities if ginger acts as the precursor for synthesizing porous carbon. Around five million tons of ginger are produced worldwide which ultimately generates a huge amount of waste. By using waste ginger as the carbon source, it is possible that new nanocarbons with surface functional groups could be prepared. In addition, this strategy offers a

safe and economical approach to the disposal of ginger waste biomass. Keeping this in mind, we report here on the synthesis of heteroatom functionalized nanoporous carbons using a solid activation approach with KOH as the activating agent. The prepared materials have been utilized for both CO_2 adsorption and energy storage applications. The optimized material showed a CO_2 adsorption capacity of 25.8 mmol/g at 0 °C (30 bar) and exhibited the highest specific capacitance of 244 F g^{-1} at the current density of 0.5 A g^{-1}.

EXPERIMENTAL

Preparation of nonporous carbon from ginger

Ginger was purchased from a local grocery store to prepare nonporous carbon. Before making the carbon materials, the purchased ginger was washed thoroughly to remove any soil residues and diced into small pieces. A specific amount of sliced ginger was transferred into an alumina boat and pyrolyzed at different temperatures (400, 500 and 600) for a period of 2 h to obtain nonporous ginger biochar. As a significant amount of ginger decomposed when we increased the temperature above 600 °C, we used the biomass prepared at 400, 500 and 600 °C for further studies.

Chemical activation of ginger biochar

The as-synthesized ginger biochar was combined with KOH in a mass ratio of 1:2, 1:3 & 1:4 and ground using a mortar and pestle to fine powder. The surface area analysis indicates that the mass ratio of 1:3 is the optimized ratio to obtain the maximum surface area. Therefore, in this manuscript, all the samples were obtained using this ratio. The mixture was maintained in a tubular furnace under N_2 for a few minutes before being ramped at a rate of 5 °C min^{-1} to 800 °C and activated for 2 h. The activated samples were crushed to fine powder and treated using 2M HCl, filtered and washed several times until the water became neutral and dried at 100 °C for 12 h. The final black powder was named GNBC4, GNBC5, and GNBC6, where GNBC denotes ginger-activated carbon and numbers 4, 5 & 6 denote pyrolysis temperatures at 400, 500 & 600 °C, respectively.

Material characterization

The nitrogen adsorption analysis was performed at the LN_2 temperature employing the ASAP 2420 surface area and porosimetry system from Micromeritics. The surface area was calculated using the Brunauer-Emmett-Teller (BET) method. The adsorption-desorption curves have been used further to obtain information on the volume and distribution of pore size. Powder X-ray diffraction (XRD) was performed with a PANalytical empyrean diffractometer to investigate the phases of the materials. Fourier Transform Infrared (FTIR) spectroscopy (Perkin Elmer) was used to study the surface functional groups. The samples were prepared by mixing a small amount of the sample with translucent potassium bromide (KBr) with a ratio of 1:200, followed by pressing the mixed sample into a disc. The scanning range is set to be 400-4,000 cm^{-1} with a resolution of 4 cm^{-1}. The surface morphology and microstructures of the material were examined using a scanning electron microscope (SEM, JSM7900F) and transmission electron microscope (TEM, JEOL F200). X-ray photoelectron spectroscopy (XPS) was employed to investigate the sample electronic structure and valence state using Kratos Axis Supra with a monochromatic Al Kα X-ray source, and the data was analyzed and deconvoluted utilizing CasaXPS software.

Methods of CO_2 adsorption

The CO_2 sorption studies were carried out using the high-pressure volumetric analyzer (HPVA) from Micromeritics. Before the analysis, samples were degassed at 200 °C for 12 h and cooled to room temperature. The measurements were carried out in the pressure range of 0-30 bar and at three different temperatures of 0, 10, and 25 °C to determine the influence of the temperature on CO_2 adsorption. The isosteric heat of adsorption was calculated using the Clausius Clapeyron equation using microactive software.

Preparation of electrodes for capacitance measurements

The model CHI760E workstation from CH instruments was used to investigate the electrochemical measurements. The sample, acetylene black, and polyvinylidene difluoride (PVDF) binder were combined in a ratio of 4:0.95:0.05 to prepare the electrode. The mixture was then gently pressed onto a nickel foam using a roller press. Three-electrode cell configurations were used for the electrochemical testing, with modified nickel mesh serving as the working electrode, Pt wire acting as the counter electrode, and Ag/AgCl serving as the reference electrode in 3 M KOH aqueous electrolyte.

Calculations used for supercapacitance measurements

The specific capacitance was calculated from the discharged curve using:

$$C_{sp} = \frac{I\Delta t}{\Delta V m}$$

where C_{sp} is the specific capacitance (F/g), I is current (A), Δt is discharging time (s), m is mass (g), and ΔV is potential (V). A two-electrode configuration was employed on the CR2032 coin cell to determine the capacitance by;

$$C = 2\frac{I\Delta t}{\Delta V m}$$

The gravimetric energy density (E, Wh/kg) and power density (P, W/kg) are calculated using:

$$E_m = \frac{1000 \times C_m \times \Delta U^2}{2 \times 3600}$$

$$P_m = \frac{3600 \times E_m}{t}$$

Where C_m (F/g) is the specific capacitance, ΔU is the potential window (V), and t is the discharge time (s)[16].

RESULTS AND DISCUSSION

The process of synthesizing ginger-activated nanoporous biocarbon is schematically shown in Figure 1. Ginger was initially pyrolyzed by varying the temperature (400, 500, and 600 °C) to prepare nonporous carbon (GPC) and further activated with KOH in the mass ratio of 1:3 (GPC:KOH) to prepare GNBC. The details of the synthesis conditions for the nonporous carbon and GNBC are summarized in Supplementary Table 1. The powder XRD patterns of the as-synthesized GNBC samples are shown in Figure 2A and Supplementary Figure 1. GNBC2-5 samples exhibit diffraction peaks at 2θ = 24.6° and 43.3°, attributed to the (002) and (100) reflections of the graphitic stackings in the carbon structure)[39]. Moreover, a shift towards a high angle in the (002) peak position with improved intensity was observed with the increase in the pyrolysis temperature to 500 °C [Supplementary Table 2], suggesting an increase in the ordering of the carbon structure. Similarly, a decrease in the interlayer spacing was also observed [Supplementary Table 2], reflecting improved carbon atom rearranged into a more graphitic structure. In contrast, the XRD pattern of GNBC6 showed a (002) peak shift towards a low angle (2θ = 23.4°) with an increase in the d-spacing to 0.381 nm, demonstrating the expansion of the graphene layers due to an increase in the pyrolysis temperature. Moreover, this could be attributed to the structural deformation of the material due to the formation of harsh activation conditions (volatilized KOH) at high temperatures as it is expected that this would create more surface functional groups due to the oxidation of carbon layers, resulting in the increase of the d-spacing[40-42].
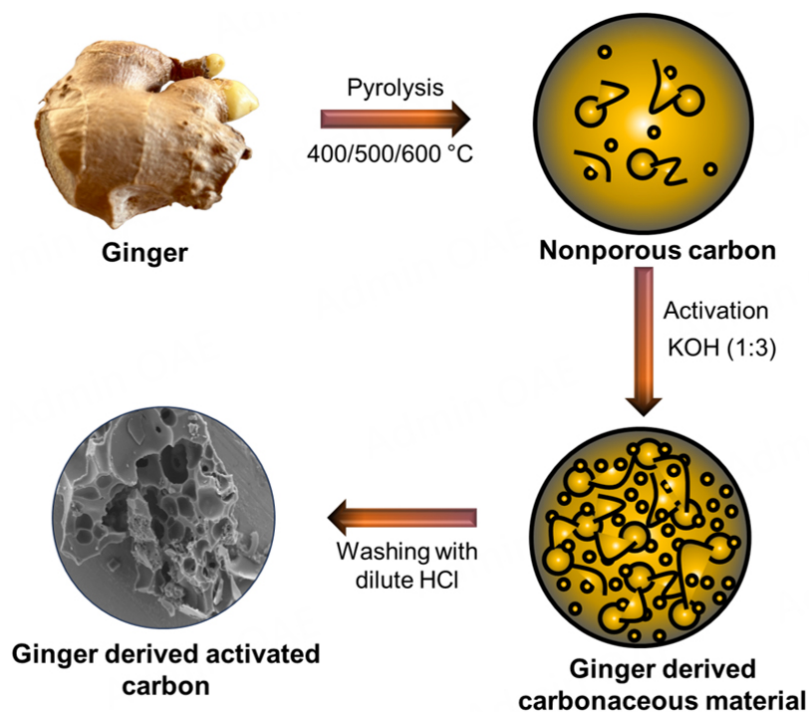
Figure 1. Schematic representation of the synthesis of porous activated carbon from ginger waste.
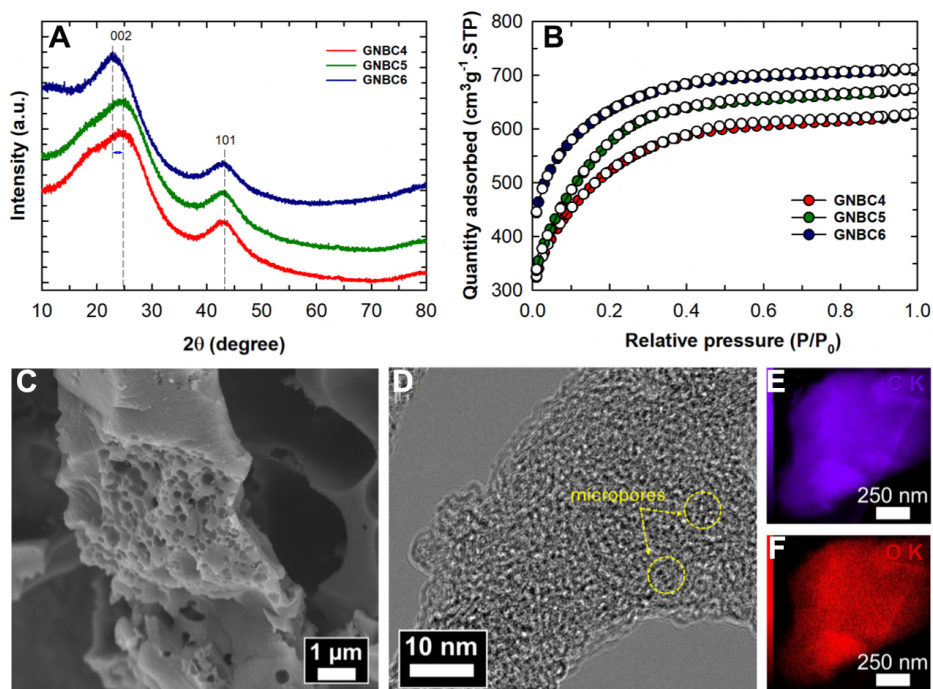

Figure 2. (A) X-ray diffraction patterns, (B) N_2 adsorption/desorption isotherms of porous activated carbon from ginger, (C) SEM, (D) TEM and EDS mapping of (E) carbon and (F) oxygen element of GNBC6 sample.

The textural properties of the GNBC materials were further investigated using the N_2 adsorption/desorption analysis and the results are shown in Figure 2B and Supplementary Figure 2. The GNBC samples exhibit a typical type I-like isotherm corresponding to the classification of the International Union of Pure and Applied Chemistry (IUPAC), reflecting the presence of micropore size distribution, and the H4-type hysteresis confirmed the presence of slit-like pores. The surface area and the pore volume of the GNBC materials increased from 1,328.1 to 2,330.6 m^2/g and 0.66 to 1.10 cm^3/g, respectively, with the pyrolysis temperature rising from 200 to 600 °C [Supplementary Table 2]. GNBC6 displayed the highest BET-specific surface area of 2,330.6 m^2/g and pore volume of 1.10 cm^3/g among all the samples. These results highlight the importance of regulating the pyrolysis temperature for enhancing the surface area and pore volume when activated with KOH. The pore diameter was analyzed using the Horvath Kawazoe method. As noticed from Supplementary Figure 3 and Supplementary Table 2, the pore diameter increased while the pyrolysis temperature grew from 400 to 500 °C (1.33 to 1.73 nm) and gradually decreased to 1.55 nm when heated at 600 °C. The presence of micropores with a size < 2 nm is highly favorable for CO_2 uptake at ambient conditions[43-45]. These results validated the importance of regulating the pyrolysis temperature during KOH activation for enhancing the surface area and pore volume. The high surface area and predominantly microporous nature of the materials are expected to be beneficial for gas adsorption and electrochemical activity.

Further structural and morphological details of GNBC were investigated using SEM and TEM analyses. The highly disordered nature of the synthesized materials, with few small pores and voids, was observed by SEM analysis [Figure 2C, Supplementary Figure 4]. A porous sheet-like structure was observed by TEM analysis of the GNBC materials, which is due to accelerated activation by KOH [Figure 2D, Supplementary Figure 5]. Furthermore, as shown in Figure 2E and F, and Supplementary Figure 6, the energy-dispersive X-ray spectroscopy (EDS) elemental mapping of GNBC samples displayed the presence of carbon (C) and oxygen (O). The elemental composition analysis for the GNBC samples showed a high amount of carbon (> 96 At.%) and less oxygen content [Supplementary Table 3].

The surface functionalities of the GNBC samples were analyzed using the FTIR spectroscopy, and the results are displayed in Figure 3A. The appearance of an extensive band from 3,200 to 3,600 cm^{-1} centered at approximately 3,421 cm^{-1}, confirmed the presence of O-H stretching vibrations which are attributed to the moisture and adsorbed hydroxyl groups. As the synthesis temperature increased, a decrease in the intensity of this band is observed due to the loss of OH functional groups at high temperatures. The bands at 1,719 and 1,612 cm^{-1} correspond to C=C and C-C stretching vibrations of -COO-, while those centered at 2,318, 1,417, and 1,137 cm^{-1} can be attributed to the C=O/C-O functional groups of the carboxylate, respectively[28]. The peaks noticed between 550 and 1,000 cm^{-1} are ascribed to the presence of aromatic C-H vibrations[46]. The difference in the intensity of the band at 1,137 cm^{-1} noticed in the samples GNBC4, GNBC5 & GNBC6 indicates the influence of pyrolysis temperature and the formation of oxygen functional groups in the alkene structure due to KOH activation[46]. Moreover, the alkene structures (C=C) functionalized with oxygen may behave more electrically conducting than samples with less oxygen functional groups[28].

The binding environment and composition of GNBC samples were further studied utilizing the XPS. Survey scans of prepared samples show peaks related to C 1s and O 1s without any noticeable impurity [Figure 3B]. The high-resolution C 1s profiles of the GNBC6 sample are fitted into three peak positions which are centered at 284.3, 285.5, and 288.6 eV binding energies, as shown in Figure 3C. Similarly, GNBC4 and GNBC5 demonstrated similar types of C 1s spectra [Supplementary Figure 7A and B]. The strong peak
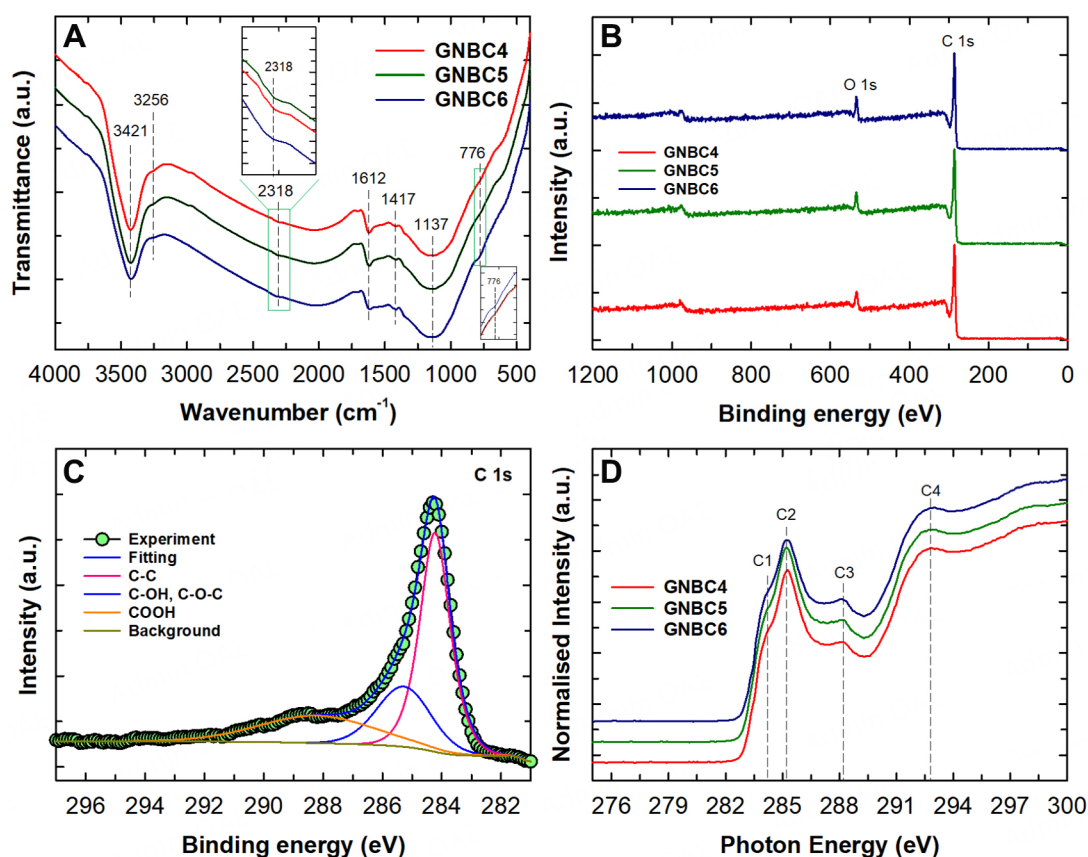
Figure 3. (A) FTIR spectra (inset shows enlarged view of peak 2,318 and 776 cm⁻¹) and (B) survey scan spectra of GNBC samples, (C) deconvoluted C 1s spectra of GNBC6 and (D) NEXAFS C K-edge spectra of GNBC samples.

at 284.3 eV is assigned to the sp^2 hybridized C-C bond, revealing the existence of graphitic carbon. The fitted peaks at 285.5 and 288.6 eV correspond to the C-O-C and O-C=O groups, and the details of the compositions are outlined in Supplementary Table 3, respectively. As shown in Supplementary Figure 8A-C, the O 1s spectra can be deconvoluted to two peaks at 532.1 and 533.9 eV, which are ascribed to the functionalities of C-O and O-C=O, respectively. The XPS analysis further reveals that the proportions of oxygen-containing functional groups (C-O) increased for the sample pyrolyzed at high temperature (GNBC6 sample), and the chemical activation could also promote high oxygen content on the carbon material [Supplementary Table 3]. The results obtained from the FTIR analysis are in good agreement with these XPS results demonstrating that the activation of the ginger biomass creates a huge amount of the surface oxygen functional groups, which may either come from the ginger biomass itself or through KOH activation due to the easy cleavage of C-O-C linkages. The C K-edge spectra obtained from the near-edge X-ray absorption fine structure (NEXAFS) analysis of GNBC4, GNBC5 & GNBC6 show four peaks represented as C1 (284.7 eV), C2 (285.2 eV), C3 (288.2 eV) and C4 (293 eV), as shown in Figure 3D. The broad bump at 284.7 eV and the sharp peak at 285.2 eV correspond to the C 1s-π* transition of C=C, and the high intensity and broadening of π* transition are observed for the samples treated at high temperatures that reflected the formation of defects in the carbon structure. The peak at 288.2 eV is ascribed to the C 1s-π* transition of C=O excitation, and the C4 feature in the range of 292 to 300 eV represents the C 1s-σ* transition of C=C resonance region, respectively[47,48].The smaller peak intensity in C1 and the broader C4 peak indicate that the graphitic plane is imperfect[49].The O K-edge spectra, as shown in Supplementary Figure 8D, display distinct peaks at 530.3 eV assigned to the O 1s-π* transition of COOH,

and 531.8 and 534.5 eV, corresponding to the O 1s-π^* transition of C=O and C-O-C, respectively[50]. The broad peak from 535 to 545 eV corresponds to the O 1s-σ^* transition of C=O, which is also consistent with the FTIR and XPS results.

The electrochemical performance of GNBC samples was investigated using the three-electrode system employing 3M KOH as the electrolyte. The cyclic voltammetry (CV) curves of GNBC4, GNBC5, and GNBC6 were measured at the scanning rate of 100 mV/s [Figure 4A]. The CV curve of GNBC6 exhibited a quasi-rectangular shape, a typical behavior of an electrical double-layer capacitor (EDLC). GNBC4 and GNBC5 samples show marginally inaccurate rectangular shapes due to the restriction in the diffusion of the ions into the layers, and this behavior could be seen at different scan rates, as shown in Supplementary Figure 9. Likewise, in the GNBC6 sample, while increasing the scan rate of the CV from 5 to 100 mV s^{-1}, the shape of the CV remained as rectangular, indicating that the ions may possibly diffuse into the pore channels despite the decreasing diffusion time. Also, as evident from the XRD, TEM, and XPS results, a disordered structure and oxygen functionalities could attract the hydrophilic electrolyte, thereby increasing the EDLC behavior.

The GCD (galvanostatic charge-discharge) tests were conducted to study the rate capabilities of the electrodes. The GCD curves measured in the current densities of 0.5 to 10 A/g from 0 to -0.8 V are shown in Supplementary Figure 10. The GNBC6 sample showed a prolonged discharge time compared to GNBC4 and GNBC5 samples at 0.5 A/g [Figure 4B], and these results are consistent with the CV. The triangular shape of the GCD curves at different current densities [Supplementary Figure 10] demonstrates ideal supercapacitive behavior of the GNBC electrodes, characterized by a minor internal resistance (IR) drop, which signifies good coulombic efficiency and excellent reversibility. The graph shown in Figure 4C illustrates the specific capacitance values of GNBC samples calculated at various current densities. Among the samples studied, GNBC6 demonstrated the highest specific capacitance of 244 F/g, followed by GNBC5 of 215 F/g and GNBC4 of 189 F/g at a current density of 0.5 A/g, respectively. Compared with other biomass activated carbons and waste derived activated carbons [Supplementary Table 4], the supercapacitance performance of the GNBC6 is much better, with an improved specific capacitance value and high stability. It could be noticed that even though the current density was varied to 10 A/g, the samples GNBC6, GNBC5, and GNBC4 displayed a specific capacitance of 125, 75 and 100 F/g. This unique performance could be due to material properties such as thin carbon sheet morphology that features a high BET-specific surface area and large pore volume, as well as the presence of micropores that offer high conductivity and better electronic transport, leading to higher capacitance at high current density. As evident from the textural properties [Supplementary Table 2], the gradual loss in the capacitance observed at high current densities in GNBC samples could be due to a hindrance in the ion diffusion caused by the pore dynamics. The electrochemical impedance spectroscopy (EIS) measurements were carried out on the GNBC electrodes to understand the mechanism of charge transfer, and the results are shown in Supplementary Figure 11. The Nyquist plots displayed a typical capacitance-like behavior in all the samples. When performing the simulation analysis using an equivalent circuit, the lowest resistance for charge transfer is observed in GNBC6 (0.69 Ω), followed by GNBC5 (0.84 Ω) and GNBC4 (0.98 Ω).

As three-electrode supercapacitance performance is exceptional in the GNBC6 sample, the sample was further evaluated in a two-electrode setup. The CV curves exhibited a nearly rectangular shape at a scan rate of 5 mV/s, which is characteristic of EDLC behavior in the carbon structure [Figure 4D]. As seen from Figure 4D, there were no significant changes observed in the CV plots as increasing the rate of scan from 5 to 100 mV s^{-1}, implying its excellent charge transfer capability, low resistance and excellent capacitance retention. Similarly, when the potential window was increased to 1.4 V, a sharp rise in electrode current was
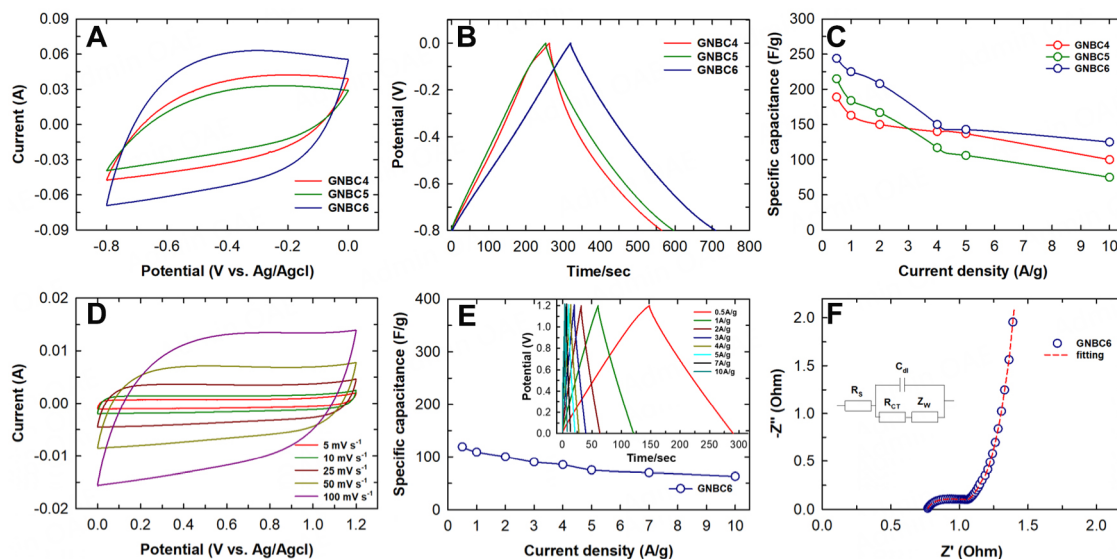
Figure 4. (A) Cyclic voltammetry curves of GNBC samples at 100 mV/s, (B) Charge-discharge profile of GNBC samples at 0.5 A/g, (C) comparison of specific capacitance at different current densities for GNBC samples, (D) CV curves measured using GNBC6 electrode at different scan rates in a two-electrode cell, (E) specific capacitance of GNBC6 at different current densities and the inset displays the corresponding GCDs, and (F) two electrode EIS spectra of GNBC6 sample.

observed, accompanied by a dramatic change in the curve's shape. This behavior suggests that the high potential caused polarization of the electrode material, leading to electrolyte decomposition[28].The relationship between voltage and time and the impact of current densities on specific capacitance values were examined through the GCD method (inset of Figure 4E). The characteristic feature of EDLC was exhibited through the triangular shape during charging and discharging, and the GNBC6 sample demonstrated a high specific capacitance of 119 F/g at 0.5 A/g and 63 F/g at 10 A/g, suggesting its promising potential for supercapacitor applications [Figure 4E]. The exceptional capacitive performance observed by the GNBC is primarily due to the minimal resistance encountered by electrolyte ions during diffusion and the confinement of ions within the pore structure, which limits the ion penetration time at higher current densities. To further investigate the ion transport and charge transfer characteristics, EIS measurements were conducted, as illustrated in Figure 4F. The Nyquist plot revealed a distinct semicircle in the high-frequency region, indicative of charge transfer resistance, and the low-frequency range displays a distinct linear line, which reflects the Warburg impedance associated with ion diffusion within the electrode material[51]. From these measurements, the equivalent series resistance (R_s) was determined to be 0.39 Ω, while the charge transfer resistance (R_{ct}) was found to be 0.75 Ω. The sample also achieved a high energy density of 23.8 Wh kg^{-1} and a power density of 8,168 W Kg^{-1} [Figure 5A]. Furthermore, the GNBC6 electrode demonstrated exceptional cyclic stability, retaining 93% of its capacitance after 10,000 continuous charge-discharge cycles at 20 A/g, with outstanding coulombic efficiency [Figure 5B]. In addition, the SEM images in Supplementary Figure 12 reveal that the GNBC6 sample exhibited no visible damage after undergoing multiple charge-discharge cycles, reinforcing its structural stability. This retention in capacity could be due to the electro-activation of the carbon material during longer charge-discharging cycling processes[16]. Ginger-derived activated carbon (GNBC6) has a hierarchical porous structure with interconnected micro, meso and macro pores. This unique structure provides a large surface area for charge storage, efficient electrolyte ion transport and short diffusion paths for ions. The interconnected pore network allows for rapid charge/discharge cycles without degradation of the structure over many cycles.
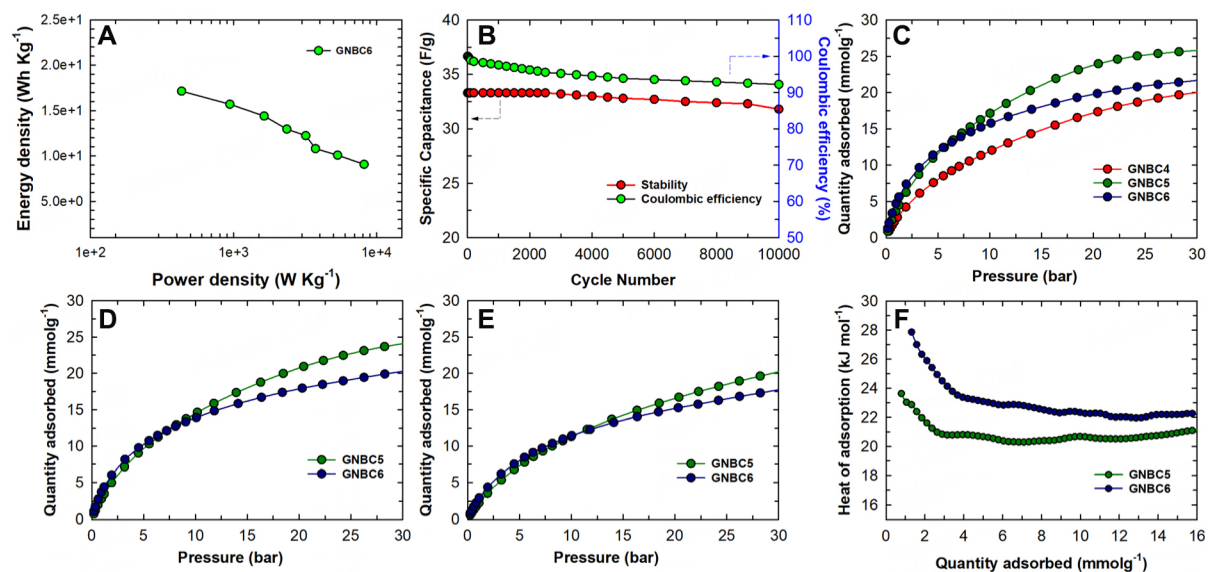
Figure 5. (A) The Ragone plot of GNBC6 sample, (B) long cycling stability and coulombic efficiency of GNBC6 sample, (C) CO_2 adsorption isotherms of GNBC4, GNBC5 and GNBC6 at 0 °C, (D and E) CO_2 adsorption isotherms of GNBC5 and GNBC6 at 10 and 25 °C, (F) Isosteric heat of adsorption of GNBC5 and GNBC6 samples.

The porous carbon materials derived from ginger biochar synthesized at the pyrolysis temperatures of 400, 500, and 600 °C demonstrated a high BET-specific surface area with enormous micropores and significantly large pore volume, which should be beneficial for enhanced gas adsorption. Therefore, the CO_2 adsorption capabilities of GNBC samples were measured at 0 °C by gradually varying the pressure from 0-30 bar. Figure 5C shows the sorption isotherms of GNBC4, GNBC5, and GNBC6 samples, demonstrating a massive rise in the adsorption of CO_2 at ambient pressure and gradually increasing as the pressure rises without any saturation. The summary of CO_2 adsorption at different pressures for the samples is shown in Supplementary Table 5. Among the samples, GNBC5 adsorbed 25.8 mmol/g of CO_2, demonstrating the highest uptake at 30 bar pressure compared to GNBC4 - 20.1 mmol/g and GNBC6 - 21.7 mmol/g. The superior CO_2 adsorption performance of GNBC5 could be attributed to the high BET-specific surface area (2,140.4 m^2/g) and pore volume (1.043 cm^3/g), where the surface area provides more sites for CO_2 molecules to interact with and the pore volume offers space for CO_2 molecules to be physically trapped[28]. Interestingly, the sample GNBC6 displayed the highest BET-specific surface area of 2,330.6 m^2/g and showed a relatively lower CO_2 uptake (21.7 mmol/g) compared to GNBC5. Thoroughly analyzing the textural parameters, we noticed that the percentage of mesopore area in sample GNBC5 (8.5%) is two-fold higher than GNBC6 (4.4%), which may lead to the higher adsorption of GNBC5 at high pressure. The results indicate that the mesopore area is crucial for increasing the CO_2 adsorption capacity under high pressures[16].However, at the low-pressure region (0 to 5 bar pressure), the sample GNBC6 displayed the highest CO_2 adsorption of 4.87 mmol/g at 1 bar, followed by GNBC5 at 3.82 mmol/g and GNBC4 at 2.65 mmol/g. The high CO_2 uptake at the low-pressure region in GNBC6 is correlated with its large proportion of micropores (95.6%) and huge micropore volume (0.99 cm^3/g). The CO_2 adsorption at low pressure is very high in micropore materials due to their small pore size, creating a large surface area for adsorption when comparing the surface area to volume ratio. Additionally, the confinement effect in micropores enhances the interactions between CO_2 molecules and the pore walls, further promoting adsorption[28].

The CO_2 adsorption was also carried out at 10 and 25 °C for GNBC5 and GNBC6 samples [Figure 5D and E] to further evaluate the influence of temperature. At elevated temperatures, the adsorption efficiency of GNBC5 and GNBC6 decreases to 24.1 and 20.2 mmol/g at 10 °C and further reduces to 20.2 and 17.7 mmol/g at 25 °C. Increasing the temperature of the adsorption process can reduce the CO_2 uptake due to several factors, such as weaker interaction between CO_2 molecules and the carbon surface and the increase in the mobility of the molecules which makes them harder to be trapped within the pores[16,18]. The significant change in the CO_2 uptake noticed in GNBC6 and GNBC5 samples arises from the adsorption kinetics that should have slowed down due to adsorbate-adsorbent interactions at relatively higher temperatures. Therefore, the strength of interactions between the CO_2 molecules and the GNBC5 and GNBC6 adsorbent materials was evaluated using the isosteric heat of adsorption (Q_{st}) calculated using the Clausius-Clapeyron equation.

As shown in Figure 5F, Q_{st} values remain between 27.9-22.3 and 23-20.9 kJ mol^{-1} for GNBC6 and GNBC5, respectively, indicating the adsorption process is physical in nature. In addition, when adsorption increases, the Q_{st} values of GNBC6 and GNBC5 decrease, indicating that during the adsorption process, more CO_2 molecules are adsorbed onto the surface, forming multiple layers of adsorption, which weakens the interaction with the surface, leading to a decrease in the Q_{st} value. Moreover, the lower strength of these interactions facilitates the easy regeneration of adsorbed gas molecules and enhances its potential for practical applications.

CONCLUSION

In this study, we sucessfully prepared nanoporous biocarbons with surface functional oxygen groups and high specific surface area from ginger biomass and applied them for high-energy supercapacitors and CO_2 capture applications. We demonstrated that the micro and mesoporous pore structures in the nanoporous biocarbon can be tuned by adjusting the pyrolysis temperatures. The developed best material showed a high BET-specific surface area of 2,330 m^2/g and a high specific capacitance of 247 F/g at a current density of 0.5 A/g in a three-electrode system which is much better than that of the activated carbon and multiwalled carbon nanotubes. It was found that the presence of rich micropores and oxygen-based functional groups, generated through the activation and from the ginger biomass, really helped to enhance the active sites, promoting the diffusion and confinement of the ions in the layers, which resulted in a high capacitance with a capacitance retention of 100% even after 2,500 cycles. In addition, the developed nanoporous biocarbon achieved an excellent CO_2 adsorption capacity of 25.8 mmol/g at 30 bar pressure. The high microporosity in the developed material facilitated a high amount of CO_2 adsorption of 4.87 mmol/g at ambient pressure and 0 °C. The enhanced performance of the synthesized materials in their intended applications could be attributed to the combined effect of their distinct porosity features. The advantages of transforming food waste to nanostructure carbon open an excellent platform for developing low-cost energy storage, CO_2 capture, and conversion materials.

DECLARATIONS

Acknowledgments

Authors' contributions

Formal analysis, writing draft and editing: Davidraj, J. M.

Conceptualization, methodology, investigation, formal analysis, writing, review and editing, visualization: Sathish, C.

Experiments: Perumalsamy, V.; Narayanan, V.; Wijerathne, B.; Yu, X.; Breese, M. B. H.

Editing: Ahmed, M. I.

Supervision, funding acquisition, conceptualization, methodology, review and editing: Yi, J.

Supervision, conceptualization, methodology, review and editing: Vinu, A.

Availability of data and materials

The data supporting the findings of this study are available within this Article and its Supplementary Material. Further data are available from the corresponding authors upon request.

Financial support and sponsorship

Conflicts of interest

Yi, J. is the guest editor of the Special Issue, while the other authors have declared that they have no conflicts of interest.

Ethical approval and consent to participate

Not applicable.

Consent For publication

Not applicable.

Copyright

REFERENCES

1. Prasankumar, T.; Salpekar, D.; Bhattacharyya, S.; et al. Biomass derived hierarchical porous carbon for supercapacitor application and dilute stream CO_2 capture. *Carbon* **2022**, *199*, 249-57. DOI
2. Muis, Z. A.; Hashim, H.; Manan, Z. A.; Taha, F. M.; Douglas, P. L. Optimal planning of renewable energy-integrated electricity generation schemes with CO_2 reduction target. *Renew. Energy.* **2010**, *35*, 2562-70. DOI
3. D'Alessandro, D. M.; Smit, B.; Long, J. R. Carbon dioxide capture: prospects for new materials. *Angew. Chem. Int. Ed.* **2010**, *49*, 6058-82. DOI PubMed
4. Senthil, C.; Lee, C. W. Biomass-derived biochar materials as sustainable energy sources for electrochemical energy storage devices. *Renew. Sustain. Energy. Rev.* **2021**, *137*, 110464. DOI
5. Liu, Z.; Yu, Q.; Zhao, Y.; et al. Silicon oxides: a promising family of anode materials for lithium-ion batteries. *Chem. Soc. Rev.* **2019**, *48*, 285-309. DOI
6. Ariga, K.; Ji, Q.; Hill, J. P.; Vinu, A. Coupling of soft technology (layer-by-layer assembly) with hard materials (mesoporous solids) to give hierarchic functional structures. *Soft. Matter.* **2009**, *5*, 3562-71. DOI
7. Singh, G.; Kim, I. Y.; Lakhi, K. S.; et al. Heteroatom functionalized activated porous biocarbons and their excellent performance for CO_2 capture at high pressure. *J. Mater. Chem. A.* **2017**, *5*, 21196-204. DOI
8. Davidraj, J. M.; Sathish, C.; Benzigar, M. R.; et al. Recent advances in food waste-derived nanoporous carbon for energy storage. *Sci. Technol. Adv. Mater.* **2024**, *25*, 2357062. DOI PubMed PMC
9. Vinu, A.; Srinivasu, P.; Takahashi, M.; Mori, T.; Balasubramanian, V. V.; Ariga, K. Controlling the textural parameters of mesoporous carbon materials. *Micropor. Mesopor. Mater.* **2007**, *100*, 20-6. DOI
10. Vinu, A. Fabrication and electrocatalytic application of nanoporous carbon material with different pore diameters. *Top. Catal.* **2010**, *53*, 291-6. DOI
11. Singh, G.; Bahadur, R.; Mee, L. J.; et al. Nanoporous activated biocarbons with high surface areas from alligator weed and their excellent performance for CO_2 capture at both low and high pressures. *Chem. Eng. J.* **2021**, *406*, 126787. DOI

12. Khosrowshahi, M. S.; Mashhadimoslem, H.; Shayesteh, H.; et al. Natural products derived porous carbons for CO_2 capture. *Adv. Sci.* **2023**, *10*, e2304289. DOI PubMed PMC

13. Singh, G.; Kim, I. Y.; Lakhi, K. S.; Srivastava, P.; Naidu, R.; Vinu, A. Single step synthesis of activated bio-carbons with a high surface area and their excellent CO_2 adsorption capacity. *Carbon* **2017**, *116*, 448-55. DOI

14. Deng, J.; Li, M.; Wang, Y. Biomass-derived carbon: synthesis and applications in energy storage and conversion. *Green. Chem.* **2016**, *18*, 4824-54. DOI

15. Sang, L. C.; Vinu, A.; Coppens, M. O. General description of the adsorption of proteins at their iso-electric point in nanoporous materials. *Langmuir* **2011**, *27*, 13828-37. DOI PubMed

16. Sathish, C.; Kothandam, G.; Selvarajan, P.; et al. Ordered mesoporous boron carbon nitrides with tunable mesopore nanoarchitectonics for energy storage and CO_2 adsorption properties. *Adv. Sci.* **2022**, *9*, e2105603. DOI PubMed PMC

17. Selvarajan, P.; Fawaz, M.; Sathish, C.; et al. Activated graphene nanoplatelets decorated with carbon nitrides for efficient electrocatalytic oxygen reduction reaction. *Adv. Energy. Sustain. Res.* **2021**, *2*, 2100104. DOI

18. Ramadass, K.; Sathish, C. I.; MariaRuban, S.; et al. Carbon nanoflakes and nanotubes from halloysite nanoclays and their superior performance in CO_2 capture and energy storage. *ACS. Appl. Mater. Interfaces.* **2020**, *12*, 11922-33. DOI

19. Lei, Z.; Lee, J. M.; Singh, G.; et al. Recent advances of layered-transition metal oxides for energy-related applications. *Energy. Stor. Mater.* **2021**, *36*, 514-50. DOI

20. Christina Mary AJ, Sathish CI, Murphin Kumar PS, Vinu A, Bose AC. Fabrication of hybrid supercapacitor device based on $NiCo_2O_4$ @$ZnCo_2O_4$ and the biomass-derived N-doped activated carbon with a honeycomb structure. *Electrochim. Acta.* **2020**, *342*, 136062. DOI

21. Singh, J.; Basu, S.; Bhunia, H. CO_2 capture by modified porous carbon adsorbents: effect of various activating agents. *J. Taiwan. Inst. Chem. Eng.* **2019**, *102*, 438-47. DOI

22. Vinu, A.; Hartmann, M. Characterization and microporosity analysis of mesoporous carbon molecular sieves by nitrogen and organics adsorption. *Catal. Today.* **2005**, *102-3*, 189-96. DOI

23. Zhu, Y.; Cao, T.; Cao, C.; Ma, X.; Xu, X.; Li, Y. A general synthetic strategy to monolayer graphene. *Nano. Res.* **2018**, *11*, 3088-95. DOI

24. Wang, X.; Zhang, Y.; Zhi, C.; et al. Three-dimensional strutted graphene grown by substrate-free sugar blowing for high-power-density supercapacitors. *Nat. Commun.* **2013**, *4*, 2905. DOI PubMed PMC

25. Liang, Y.; Li, Y.; Wang, H.; et al. Co_3O_4 nanocrystals on graphene as a synergistic catalyst for oxygen reduction reaction. *Nat. Mater.* **2011**, *10*, 780-6. DOI

26. Li, X.; Zhang, G.; Bai, X.; et al. Highly conducting graphene sheets and Langmuir-Blodgett films. *Nat. Nanotechnol.* **2008**, *3*, 538-42. DOI

27. Stankovich, S.; Dikin, D. A.; Dommett, G. H. B.; et al. Graphene-based composite materials. *Nature* **2006**, *442*, 282-6. DOI

28. Geng, X.; Singh, G.; Sathish, C. I.; et al. Biomass derived nanoarchitectonics of porous carbon with tunable oxygen functionalities and hierarchical structures and their superior performance in CO_2 adsorption and energy storage. *Carbon* **2023**, *214*, 118347. DOI

29. Joseph, S.; Kempaiah, D. M.; Benzigar, M. R.; et al. Highly ordered mesoporous carbons with high specific surface area from carbonated soft drink for supercapacitor application. *Micropor. Mesopor. Mater.* **2019**, *280*, 337-46. DOI

30. Ismail, I. S.; Singh, G.; Smith, P.; et al. Oxygen functionalized porous activated biocarbons with high surface area derived from grape marc for enhanced capture of CO_2 at elevated-pressure. *Carbon* **2020**, *160*, 113-24. DOI

31. Singh, G.; Lakhi, K. S.; Sathish, C.; Ramadass, K.; Yang, J. H.; Vinu, A. Oxygen-functionalized mesoporous activated carbons derived from casein and their superior CO_2 adsorption capacity at both low- and high-pressure regimes. *ACS. Appl. Nano. Mater.* **2019**, *2*, 1604-13. DOI

32. Nagaraju, G.; Cha, S. M.; Yu, J. S. Ultrathin nickel hydroxide nanosheet arrays grafted biomass-derived honeycomb-like porous carbon with improved electrochemical performance as a supercapacitive material. *Sci. Rep.* **2017**, *7*, 45201. DOI PubMed PMC

33. Prabu, S.; Chiang, K. Y. Natural bio-waste-derived 3D N/O self-doped heteroatom honeycomb-like porous carbon with tuned huge surface area for high-performance supercapacitor. *Chemosphere* **2024**, *361*, 142400. DOI PubMed

34. Nallapureddy, J.; Sreekanth, T. V. M.; Pallavolu, M. R.; et al. Strategic way of synthesizing heteroatom-doped carbon nano-onions using waste chicken fat oil for energy storage devices. *ACS. Appl. Mater. Interfaces.* **2024**, *16*, 23334-43. DOI

35. Liu, J.; Thallapally, P. K.; McGrail, B. P.; Brown, D. R.; Liu, J. Progress in adsorption-based CO_2 capture by metal-organic frameworks. *Chem. Soc. Rev.* **2012**, *41*, 2308-22. DOI PubMed

36. Patel, H. A.; Karadas, F.; Canlier, A.; et al. High capacity carbon dioxide adsorption by inexpensive covalent organic polymers. *J. Mater. Chem.* **2012**, *22*, 8431-7. DOI

37. Su, F.; Lu, C. CO_2 capture from gas stream by zeolite 13X using a dual-column temperature/vacuum swing adsorption. *Energy. Environ. Sci.* **2012**, *5*, 9021-7. DOI

38. Heydari-Gorji, A.; Belmabkhout, Y.; Sayari, A. Polyethylenimine-impregnated mesoporous silica: effect of amine loading and surface alkyl chains on CO_2 adsorption. *Langmuir* **2011**, *27*, 12411-6. DOI PubMed

39. Lua, A. C.; Yang, T. Effect of activation temperature on the textural and chemical properties of potassium hydroxide activated carbon prepared from pistachio-nut shell. *J. Colloid. Interface. Sci.* **2004**, *274*, 594-601. DOI

40. Ramirez, N.; Sardella, F.; Deiana, C.; et al. Capacitive behavior of activated carbons obtained from coffee husk. *RSC. Adv.* **2020**, *10*, 38097-106. DOI PubMed PMC

41.　Yang, H.; Ye, S.; Zhou, J.; Liang, T. Biomass-derived porous carbon materials for supercapacitor. *Front. Chem.* **2019**, *7*, 274.　DOI　PubMed　PMC

42.　Girgis, B. S.; Temerk, Y. M.; Gadelrab, M. M.; Abdullah, I. D. X-ray diffraction patterns of activated carbons prepared under various conditions. *Carbon. Lett.* **2007**, *8*, 95-100.　DOI

43.　Marco-Lozar, J. P.; Kunowsky, M.; Suárez-García, F.; Linares-Solano, A. Sorbent design for CO_2 capture under different flue gas conditions. *Carbon* **2014**, *72*, 125-34.　DOI

44.　Lee, S. Y.; Park, S. J. Determination of the optimal pore size for improved CO_2 adsorption in activated carbon fibers. *J. Colloid. Interface. Sci.* **2013**, *389*, 230-5.　DOI　PubMed

45.　Casco, M. E.; Martínez-Escandell, M.; Silvestre-Albero, J.; Rodríguez-Reinoso, F. Effect of the porous structure in carbon materials for CO_2 capture at atmospheric and high-pressure. *Carbon* **2014**, *67*, 230-5.　DOI

46.　Li, C.; Li, Y.; Shao, Y.; et al. Activation of biomass with volatilized KOH. *Green. Chem.* **2023**, *25*, 2825-39.　DOI

47.　Heymann, K.; Lehmann, J.; Solomon, D.; Schmidt, M. W. I.; Regier, T. C 1s K-edge near edge X-ray absorption fine structure (NEXAFS) spectroscopy for characterizing functional group chemistry of black carbon. *Org. Geochem.* **2011**, *42*, 1055-64.　DOI

48.　Latham, K. G.; Simone, M. I.; Dose, W. M.; Allen, J. A.; Donne, S. W. Synchrotron based NEXAFS study on nitrogen doped hydrothermal carbon: insights into surface functionalities and formation mechanisms. *Carbon* **2017**, *114*, 566-78.　DOI

49.　Kikuma, J.; Yoneyama, K.; Nomura, M.; et al. Surface analysis of CVD carbon using NEXAFS, XPS and TEM. *J. Electron. Spectrosc. Relat. Phenom.* **1998**, *88-91*, 919-25.　DOI

50.　Ganguly, A.; Sharma, S.; Papakonstantinou, P.; Hamilton, J. Probing the thermal deoxygenation of graphene oxide using high-resolution in situ X-ray-based spectroscopies. *J. Phys. Chem. C.* **2011**, *115*, 17009-19.　DOI

51.　Farma, R.; Indriani, A.; Apriyani, I. Hierarchical-nanofiber structure of biomass-derived carbon framework with direct CO_2 activation for symmetrical supercapacitor electrodes. *J. Mater. Sci. Mater. Electron.* **2023**, *34*, 81.　DOI